A Split-Sensor Light Field Camera for Extended Depth of Field and Superresolution

Paolo Favaro

Heriot-Watt University, Riccarton, Edinburgh, UK;

ABSTRACT

It has been shown that the original light field camera behaves the opposite of a conventional one: Image blur decays away from a certain plane in space, a property that is called *inverted* depth of field.[1] Moreover, the blur at such *out of focus* plane is bounded from above. This property allows the light field camera to exceed the depth of field of conventional imaging systems as well as that of other computational devices. In this paper, we propose a novel design to further improve the light field camera. The proposed system can drastically reduce the loss in resolution at the out of focus plane while retaining the advantages of the original camera design. We introduce a beam splitter (prism or glass) to provide the same field of view on two halves of the sensor. We also split a microlens array in two halves matching the sensor partition. The focal length of the microlenses in one half can be different from those of the other half. In the geometric optics approximation this architecture ensures that each half of the sensor can measure light ray samples with different (and partially complementary) aliasing properties.

Keywords: Plenoptic camera, beam splitter, extended depth of field, light field

1. INTRODUCTION

The original design of the *plenoptic* or *light field* (LF) camera consists of a conventional camera with an additional microlens array between the sensor and the main optics. This modification has been used to obtain 3D from a single image,[2] to demonstrate *digital refocusing*,[3] to recover transparent 3D objects in microscopy[4] and for full-frame light field reconstruction and rendering.[1, 5, 6] One of the most important features of this camera is that it enables all these applications from a single snapshot, and hence it can be easily applied to scenes with moving objects. Moreover, the LF camera design enables a dramatic depth of field (DoF) extension. In a LF camera blur is low everywhere except for a small band around a plane in space where it grows up to a certain bound[1] (about the size of one microlens) as shown in Fig. 1. This limitation is not dramatically severe and one can adjust settings so that all objects are away from the out of focus plane. However, there is a restricted selection of settings that allow to do so before other limitations become prominent as explained in work by Bishop and Favaro.[1] Hence, to provide more flexibility in the LF camera settings, we propose a novel design that we call *split-sensor* light field camera. Our strategy is to sample the same field of view of the scene with two different plenoptic cameras. To enable the sharing of the same field of view, we introduce 2 beam splitters between the microlens array and the main optics (see Fig. 1, right). The final result is that the same view is projected onto two separate halves of the sensor. Each half of the sensor corresponds to a different focal plane in space. This allows to capture image samples of the scene that contain complementary information so that when one half of the sensor experiences a loss of resolution (due to objects at the out of focus plane), the other half of the sensor captures sharp images. Then, by exploiting the fact that LF of natural scenes generally satisfy models of limited complexity,[7] such as the Lambertian model, it is possible to combine the samples with a superresolution (SR) algorithm to recover a full sensor resolution image.[1] Notice that solving the SR problem requires recovering the depth map of the scene, which we do not investigate in this paper.

Further author information: (Send correspondence to P. Favaro)
P. Favaro: E-mail: paolo.favaro@gmail.com, Telephone: +44 131 451 3773

Optics, Photonics, and Digital Technologies for Multimedia Applications II, edited by
Peter Schelkens, Touradj Ebrahimi, Gabriel Cristóbal, Frédéric Truchetet, Pasi Saarikko,
Proc. of SPIE Vol. 8436, 843602 · © 2012 SPIE · CCC code: 0277-786X/12/$18 · doi: 10.1117/12.924927

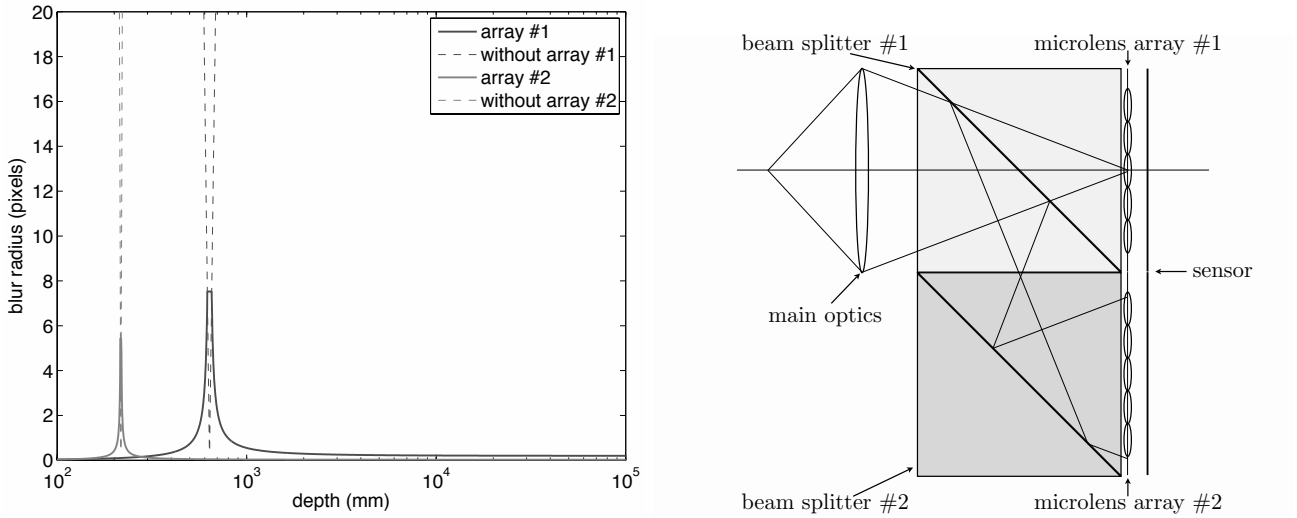

Figure 1. The proposed split-sensor light field camera. Left: Blur analysis. On the abscissa axis we show the distance of objects from the camera in millimeters in log scale. On the ordinate axis we show the blur on the sensor in pixels. Images generated with blur radii less than 0.5 pixels are considered sharp. The solid line plots correspond to the two light field camera shown to the right (also see Sec. 4). The solid line with the rightmost peak describes the blur measured on the top partition of the sensor (due to the microlens array #1). The solid line with the leftmost peak describes the blur measured on the bottom half of the sensor (due to the microlens array #2). Notice that the extra light path needed to reach the bottom half of the sensor results in a out of focus plane that is closer to the camera than the corresponding plane for the top half of the sensor. Also, the maximum blur in both cases is bound from above and corresponds to the maximum diameter allowed under a single microlens. The dashed lines show the blur in images captured under the same settings, but without the microlenses. One can see that the split-sensor design is equivalent to overlapping two light field cameras with different internal parameters (see Fig. 4). Right: Schematic of the proposed camera. Two beam splitters are placed between the microlenses and the main optics. Notice that the bottom beam splitter is only reflective. Also, the aperture of the main optics (top-left) matches only half of the sensor size (rightmost plane).

1.1. Prior Work

This work relates to *computational photography*, an emerging field encompassing several methods to enhance the capabilities and overcome limitations of standard digital photography by jointly designing imaging devices and reconstruction algorithms. In particular, we are interested in the *plenoptic camera*, which is one of the first devices based on the principles of integral photography[8] that have been proposed in computer vision by Adelson and Wang[2] to infer depth from a single snapshot. Similar architectures can be engineered into a single package chip and have been demonstrated for both image and 3D reconstruction.[9] In its original design, the plenoptic camera consists of a camera body with a single main lens, and a lenticular array at its focal plane.[3] To date, the most complete survey on computation cameras and light field imaging can be found in reviews by Wetzstein *et al.*[10] and by Zhou and Nayar.[11] While the former review classifies computational techniques based on five characterizations of the plenoptic function (*i.e.*, dynamic range, spatial resolution, frequency, angular resolution, and time), the latter review classifies such techniques based on how the plenoptic function is reconstructed (*i.e.*, coding approaches or camera design). In addition to the above surveys, light field imaging with several camera architectures is described and analyzed in several articles (*e.g.*, see Levin *et al.*[12] and Ihrke *et al.*[13]).

Alternatives to the plenoptic camera have been proposed: For example, the *programmable aperture* camera[14] captures LF data by multiplexing views of the scene. While this approach allows recovery of images at full sensor resolution, the price to pay is a long exposure time or a low signal to noise ratio (SNR). More importantly, the scene has to be static. If motion occurs, views must be aligned, which adds further complexity and computational cost to the system. Veeraraghavan *et al.*[15] propose an alternative ingenious design, the heterodyne camera, where the LF is modulated using an attenuating mask close to the sensor plane. This system has a considerable limitation: The SNR is much reduced due to light attenuation at the mask. Some recent improvements that

reduce the loss have been proposed, but they still compare unfavorably with the light field camera.[13] Georgiev and Intwala[16] suggest variants on the LF camera design. Instead of internal microlenses, they add optics external to the main lens, such as arrays of positive/negative lenses or prisms. These designs tend to suffer from higher order optical aberrations. Ben-Ezra *et al.*[17] propose a novel resolution-enhancing design, which captures multiple frames, shifted by known sub-pixel amounts. To achieve this without motion blur, micro-actuators instantaneously shift the sensor before capturing each frame. The frames are combined to reconstruct a single high resolution image. Similarly to,[14] this method trades off exposure time for spatial resolution and hence is not ideal for capturing moving objects.

Other optical designs such as wavefront coding[18] and focal sweep[19] have been proposed to recover all-focused images via *approximately* depth-invariant blurs that are easily deconvolved. However, such approaches are not considered in this paper as they cannot retrieve 3D of a scene, and do not give the possibility of refocusing. Furthermore, these systems can only work with Lambertian scenes. On the contrary, the LF camera can always be used for specular surfaces, albeit with a loss in spatial resolution.

2. LIMITATIONS OF THE PLENOPTIC CAMERA

The original design of the plenoptic camera can be seen in Fig. 1, on the right, by suppressing the beam splitters and the lower half (shaded in orange) of both the microlens array and the sensor. It consists of a conventional camera with an additional array of microlenses placed near the sensor and behind the front optics. The insertion of a microlens array in a conventional camera allows to separate incoming light not only based on where it originates, but also based on which direction it travels along. Thus, it is possible to directly measure samples of the so-called light field. If objects are Lambertian, *i.e.*, they reflect light with equal brightness regardless of the viewing direction, then one can use all the samples only for image reconstruction and essentially extend the depth of field of the camera. As shown in Fig. 1, the blur produced by a conventional camera is small only close to the focal plane in space (*e.g.*, 642mm for the first microlens array or 217mm for the second array); however, the blur produced by a LF camera behaves exactly in the opposite way: It is small everywhere, except for locations close to the focal plane (of the conventional camera). Furthermore, while the blur of a conventional camera can grow unbounded, the blur of a LF camera is automatically bounded by the size of the microlenses. This behavior has immediate consequences on the quality of the samples and the corresponding reconstruction of an all-in-focus image of the scene as shown in Fig. 2 (courtesy of Bishop and Favaro[1]). In this scene the focal plane of the conventional camera is placed in the middle of the image (i.e., at the bottom of the fluid dynamics book) and one can see a "pixelization" effect, *i.e.*, a loss of resolution of the superresolved image at such location. As mentioned earlier on, this effect is due to the specific design of the plenoptic camera. Notice that the loss of resolution is fixed by the microlens array size. Indeed, the worst case scenario is when each microlens is completely blurred and hence provides just one new sample to the superresolved image. However, the detailed analysis of the loss in the spatial resolution in a plenoptic camera is more complex and articulated. Firstly, the superresolution reconstruction is possible only if the 3D surface of the scene is available. In fact, the albedo of a 3D point on the surface of a Lambertian object can be reconstructed by using the light measured along any of the outgoing directions. Therefore, the image reconstruction accuracy depends on the accuracy of the depth reconstruction. Secondly, the distribution of samples varies with depth. One can show that an image reconstructed on a uniform grid will exhibit an increasing loss of resolution for objects far away from the camera and for a certain set of planes in space (the planes where samples coincide[1]). Our proposed design is an attempt to overcome these limitations while retaining the advantages of the original design. In the next section we introduce the notation, which mostly follows the work of Bishop and Favaro.[1] The reader already familiar with such notation can skip the next section.

3. NOTATION

In our design there is a single microlens array and a single sensor. The microlens array, however, is split in two halves each with a different focal length. The top half of the sensor can be considered as a traditional light field camera, as 50% of the light passes through the first prism without being deflected and the other 50% is redirected towards the second beam splitter. The second prism then completely reflects (as a mirror) the light towards the bottom half of the sensor. The bottom half of the sensor is therefore equivalent to a traditional light

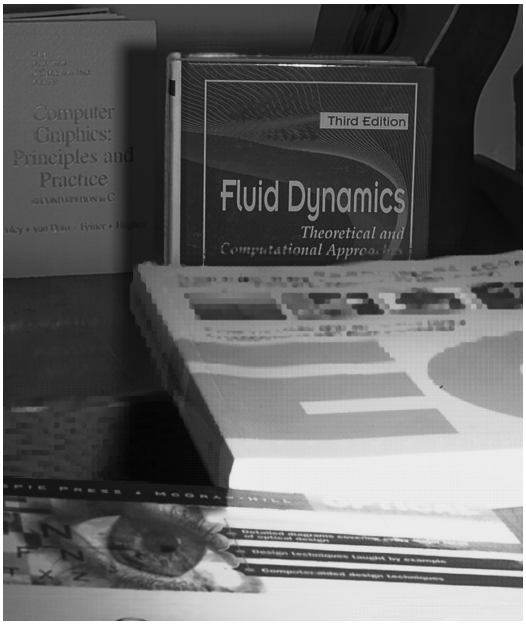

Figure 2. Reconstruction of a scene under the Lambertian model (image kindly provided by Bishop and Favaro[1] and with permission of IEEE, which holds the copyright). Notice that the central horizontal band appears pixelized. This is the location of the out of focus plane in the light field camera. Reconstruction of pixel intensities at those locations is not possible with a traditional light field camera. The proposed split-sensor scheme addresses this limitation.

field camera (as in the top half), but with additional internal spacing between the main optics and the microlens array. Because the chosen prisms are square and have a 45 degrees slope inside, such additional distance is equal to one side of the prism. Hence, let us recall the notation used for a single light field camera and let us distinguish the two halves of the microlens array and of the sensor by adding a 1 or a 2 as subscript to the parameters relative to the first or the second half respectively.

First of all, let us start by defining the parameters for a single light field camera. For simplicity, as in prior work,[1] we consider working entirely inside the camera with the conjugate images of objects in space. An object at a distance $z \in \mathbb{R}$ from the main optics has a unique corresponding *conjugate* point inside the camera at a distance $z' \in \mathbb{R}$ from the main optics due to the *thin lens law* (in Fig. 4, left, the chosen point in space results in a z' equal to the spacing v')

$$z' = \frac{Fz}{z - F} \tag{1}$$

where F denotes the main lens focal length. Therefore, a surface in space corresponds to a conjugate surface $z'(\boldsymbol{u})$ inside the camera, parameterized by coordinates $\boldsymbol{u} \in \mathbb{R}^2$ on the first microlens plane. The first microlens array is located at a distance v' behind the main lens and the second one at a distance $v' + \rho$, where ρ is one side of the beam splitter. Each microlens has a diameter of d. The sensor is then located at a distance v from the microlens array.

In our approximation, the light field is a 4D function that defines light intensity reflected at a 3D point on an object and along a certain direction. The parameterization of the 4D LF is shown in Fig. 3. Notice that this illustration shows only the arrangement of optics and sensor inside one plenoptic camera. On the left we have the main optics; at a distance v' we have the microlens array (lenslets dimensions are exaggerated for illustration purposes); finally, at a distance v from the microlens array we have the sensor. We parametrize it with respect to the 2D spatial coordinates $\boldsymbol{u}$ and the 2D angular coordinates $\boldsymbol{\theta}$. In our representation, the 2D spatial coordinates $\boldsymbol{u}$ are defined on the microlens array. This is the plane where we also reconstruct the reflectance of the scene. If we knew the depth map of the scene, $\boldsymbol{u}$ would identify a 3D point on a surface in space. The continuous 2D angular coordinates $\boldsymbol{\theta} \in \Theta \subset \mathbb{R}^2$ are locally defined on the sensor plane relative to each microlens, and have a

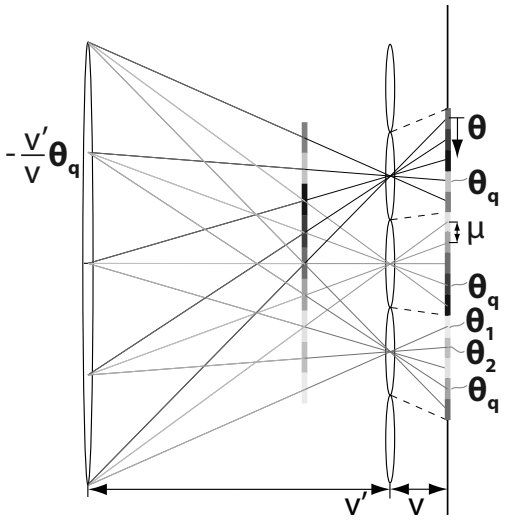

Figure 3. Coordinates and sampling in the plenoptic camera (image kindly provided by Bishop and Favaro[1] and with permission of IEEE, which holds the copyright). Pixels under each microlens are mapped onto points on the main lens. The measured intensity, when the microlens diameter is negligible, is the sample collected along the ray intersecting the conjugate image of the object (here visualized as a vertical plane between the main lens and the microlens array).

one-to-one mapping with coordinates on the main lens (see $-\frac{v'}{v}\boldsymbol{\theta_q}$ in Fig. 3). Θ defines the set of $\boldsymbol{\theta}$ contained within the main lens aperture's projection onto the sensor, which we assume square for simplicity. $\boldsymbol{\theta}$ under each microlens is defined so that it projects to the same main lens position. Its discretized version is $\boldsymbol{\theta_q} \doteq \mu \boldsymbol{q}$, where μ is the pixel width, $\boldsymbol{q} = [q_1, q_2]^T$ and $q_1, q_2 \in \{-\lfloor (Q-1)/2 \rfloor, \ldots, 0, \ldots, +\lfloor (Q-1)/2 \rfloor\}$, with $\lfloor a \rfloor$ the floor operator. $\boldsymbol{\theta_q}$ indexes the sensor pixels relative to each microlens, so that we have a total of Q^2 angular samples (when Q is odd).

4. SPLIT-SENSOR PLENOPTIC CAMERA

To address the limitations of the original plenoptic camera design, we propose a modified architecture, which we call the *split-sensor plenoptic camera* and is illustrated in Fig. 1. In this section we analyze the proposed system by using the same scheme proposed in Bishop and Favaro.[1] We first show the ray space sampling, and then exploit several parameters that define the performance of the proposed system: repetitions, blur, and coincidence of samples.

4.1. Ray space representation

Fig. 4, left, shows 3 Lambertian objects (green, red, and blue) being imaged with the proposed camera. The conjugate image of the red object is at the plane of the first microlens array. The pair microlens array #1 and corresponding sensor define the first LF camera and the other pair defines the second LF camera. Notice that we carry out the analysis of the system in Fig. 1 by eliminating the prisms and by positioning the second LF camera further away from the main lens by a spacing ρ.

In Fig. 4, right, we show an alternate view of sampling, aliasing and blurring effects in the split-sensor light field camera, via the (2D) ray space representation used by Levin *et al.*[7] In our version we use the internal camera coordinates: $\boldsymbol{u}$ for the abscissa axis (spatial) and the projection of $\boldsymbol{\theta}$ onto the main lens for the ordinate axis (angular). A point in this space represents a ray through the corresponding positions on the main lens and first microlens array; a ray with constant color in this space corresponds to the set of all pairs $(\boldsymbol{u}, \boldsymbol{\theta})$ that define rays through a conjugate point in the plot to the left (*e.g.*, the vertical red rays are points on the microlens array, conjugate to the main lens plane in focus in space; different slopes represent other depths, with the same colors as the planes in Fig. 4, left). Each gray parallelogram indicates the rays in the LF that a sensor pixel in the top half integrates. Similarly, the yellow parallelogram indicate the rays in the LF that a sensor pixel in the bottom

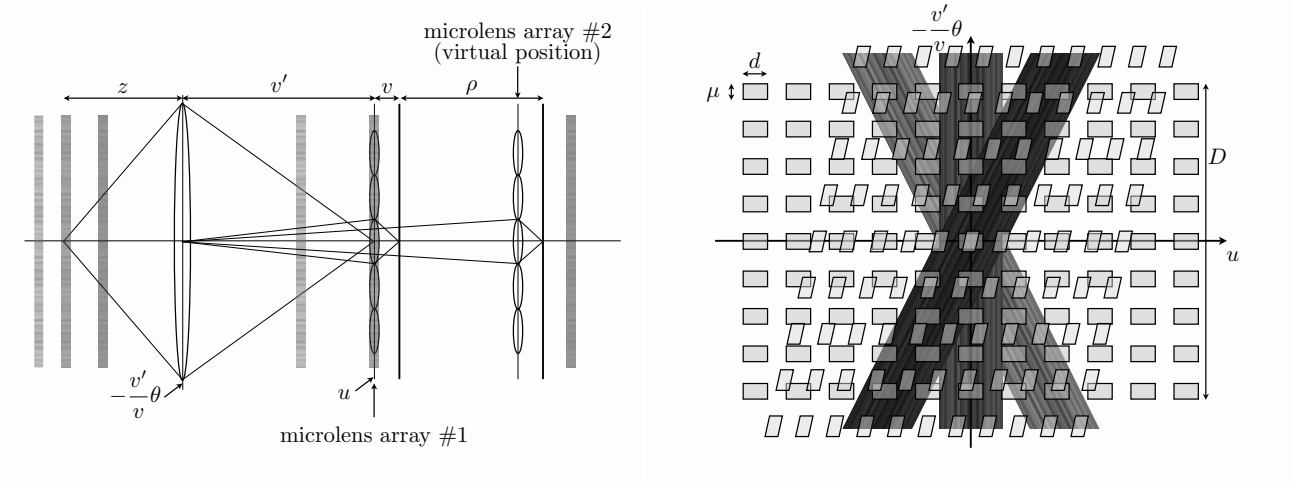

(a) equivalent schematic of the proposed light field camera (b) sampling pattern of the proposed light field camera

Figure 4. Sampling patterns of the proposed split-sensor light field camera. (a) If we ignore the second microlens array, the schematic is identical to the original light field camera. The use of beam splitters is equivalent to consider a shorter light path to the bottom half of the sensor. Notice that the second microlens array (corresponding to the bottom half of the sensor) has lenslets with different focal length than the lenslets in the first microlens array (so that the bottom half of the sensor is still in focus at the main lens). (b) the sampling array of the first microlens array is shown in rectangles and the sampling array of the second microlens array is shown in parallelograms (slanted rectangles). The three objects (fronto-parallel planes) in the schematic to the left, one between the main lens and the first array, one at the first array and one to the right of the second array, correspond to the negative slope, vertical slope, and positive slope objects respectively in the image to the right.

half integrates; their shear angle corresponds to the conjugate plane the microlenses are focused on. A column of parallelograms is the collection of samples under one microlens.

Gaps between parallelograms are due to pixel fill-factor vertically, and microlens apertures horizontally. Notice that the red object (vertical lines) appears completely blurred in the top LF camera as all the pixels under one microlens (*i.e.*, along one column) integrate exactly the same texture content. To achieve the highest sampling accuracy achievable, the gray or yellow parallelograms should not be aligned along a ray of constant intensity.

4.2. Main lens defocus radii

With reference to Fig. 6, the cone of rays starting from P and passing through the aperture $D = \|AB\|$ causes a blur on the first microlens array plane. This blur region determines how many microlenses capture light from P. Under the Lambertian assumption, P casts the same light on each microlens, and this results in multiple copies of the light reflected at P that can be used to reconstruct the LF. By approximating this blur by a Pillbox with side $H_1 \geq 0$ (*i.e.*, the unit volume box,* $h(\boldsymbol{u}) = \frac{1}{4H_1^2}$ for $-H_1 \leq u_1, u_2 \leq H_1$ and 0 otherwise), the main lens blur side is

$$H_1 = \frac{Dv'}{2}\left|\frac{1}{z'} - \frac{1}{v'}\right|. \tag{2}$$

For simplicity, consider writing ρ as a multiple of v', *i.e.*, $\rho = \kappa v'$ for some coefficient $\kappa > 0$. Then, the second main lens blur can be written as

$$H_2 = \frac{Dv'}{2}\left|\frac{1+\kappa}{z'} - \frac{1}{v'}\right|. \tag{3}$$

*Notice that in this analysis we consider a square main lens aperture. However, the analysis can be easily extended to other shapes, such as the more conventional disk.

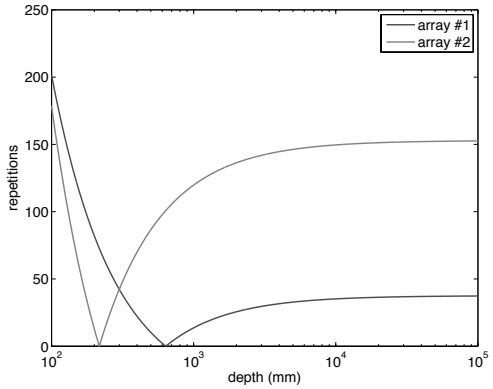

Figure 5. Number of repetitions under each microlens array. Notice that where the number of repetitions drops for one LF camera, it is high for the other LF camera. Ideally, the number of repetitions should not grow too high. To limit the number of repetitions, the parameter κ should be small. However, the current setup fixes the relative position of the two microlens arrays and result in a large κ. To avoid this rigid arrangement one can use only one beam splitter and two microlens arrays with two sensors placed at its two beam-exiting sides with the desired spacing. This choice, allows any κ, but, however, results in a more expensive device.

To characterize the number of repetitions of the same pattern in the scene, we must count how many microlenses fall inside the main lens blur square. Therefore, in each direction we have

$$\#\text{repetitions top} = \frac{2H_1}{d} = \frac{Dv'}{d}\left|\frac{1}{z'} - \frac{1}{v'}\right| \tag{4}$$

$$\#\text{repetitions bottom} = \frac{2H_2}{d} = \frac{Dv'}{d}\left|\frac{1+\kappa}{z'} - \frac{1}{v'}\right|. \tag{5}$$

An example of repetitions computed with the same settings in Fig. 1 is shown in Fig. 5. This ratio is also evident in the ray space (Fig. 4) by considering how many columns of either the first or the second array one constant intensity ray (of an object) covers. We know that the number of repetitions is important to estimate the depth map of the scene.

4.3. Microlens blurs

The blur of a microlens in the first array that is fully covered by the main lens blur is a pillbox, due to the circular microlens aperture, with radius:

$$b_1 = \frac{dv}{2}\left|\frac{1}{f_1} - \frac{1}{v'-z'} - \frac{1}{v}\right|, \tag{6}$$

where f_1 is the focal length of lenslets in the first array. Similarly, the blur under the second array can be written as

$$b_2 = \frac{dv}{2}\left|\frac{1}{f_2} - \frac{1}{v'(1+\kappa)-z'} - \frac{1}{v}\right|, \tag{7}$$

where f_2 is the focal length of lenslets in the second array. In Fig. 4, the microlens blur can be evaluated graphically as the projection of the intersection between the constant-intensity ray of an object and one column of pixels under one microlens. Also, a plot of the blurs under each microlens array is shown in Fig. 1. As shown in Fig. 6, the arrangement of the optics is such that when one LF camera is out of focus, the other is sharp and vice versa.

Notice that the two microlens arrays have separate out of focus blur locations and therefore one array can compensate for the loss in resolution due to the other. In terms of the ray space, changes of v correspond to a vertical shear of each integration region. We consider Ng's[3] setting (microlenses focused on the main lens), so

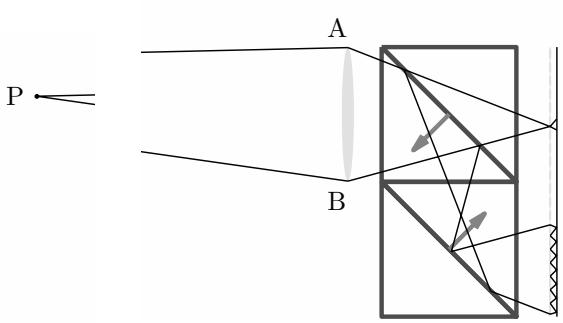

(a) Microlens array #1 is out of focus

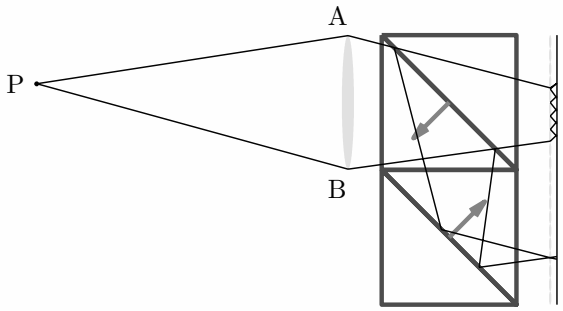

(b) Microlens array #2 is out of focus

Figure 6. Blur due to the main lens and to the microlenses for two objects. (a) The conjugate image of the object P lies on the first microlens array, thus causing high blur in the top half of the sensor. However, the second half collects sharp samples. (b) The conjugate image of the object P lies on the second microlens array, thus causing high blur in the bottom half of the sensor. In this case the top half of the sensor measures sharp pixels.

that the regions become rectangular for the first array. In the second array the integration regions corresponding to each pixel are skewed. A point on the sensor of the second LF camera collects all the rays deflected from the microlens and coming from a single location on the main lens (see Fig. 4, left). This means that the angular coordinate does not change, but the spatial coordinate does. if now we integrate rays within the area of a pixel, the spatial and angular coordinates will increase or decrease jointly. This creates the positive slope skewness of the yellow integration regions.

4.4. Coincidence of samples

Samples from different microlenses may intersect in space on some fronto-parallel planes. When this happens, we call the samples on these planes *coincident* as on these planes the imaging device collects the same samples. This can be useful for depth estimation, but from the point of view of texture, there is a loss in resolution. In Fig. 4, this degeneracy corresponds to a ray passing through exactly the same point in a parallelogram from different columns of microlens pixels.

To have an exact replica of a sample under two microlenses in the same array, the sample must simultaneously project on two discrete pixel coordinates. By considering two microlenses separated by Nd, with $N \in \mathbb{Z}$, then the coordinate under the first microlens must correspond to a coordinate $Nd\frac{z'}{v'}\frac{v}{v'-z'} = T$, where $T \in \mathbb{Z}$. Also, for the corresponding pixel to be fully under a microlens, $T < \frac{\mu Q}{2}$. By substituting the expression for T, we see that such microlenses must satisfy $N < \frac{\mu Q v'(v'-z')}{2dz'v} = \frac{1}{2}\#\text{repetitions}$. Moreover, the corresponding depths are those such that $\frac{z'}{v'}\frac{v}{v'-z'} = \frac{T}{Nd}$ with N and T integers. Finally, we can also determine the total number of genuinely new samples by analyzing the overlap between different microlenses. When $\exists\ N_i, T_i \geq 1,\ i = 1, 2$, coprime (if

not, we could always find additional matching samples), then the total number is

$$\text{new pixels from array } \#1 = [N_1Q + T_1(K_1 - N_1)][N_1Q + T(K_2 - N_1)] \quad (8)$$

$$\text{new pixels from array } \#2 = [N_2Q + T_2(K_1 - N)_2][N_2Q + T(K_2 - N_2)]. \quad (9)$$

5. CONCLUSIONS

We have introduced a novel plenoptic camera by introducing 2 beam splitters. The splitters provide the same field of view on two halves of the sensor. The proposed architecture gains resolution where the traditional LF camera fails. We compute several parameters that have been used to characterize the performance of light field cameras. In future work we plan to implement and assess the experimental performance of the proposed imaging device.

ACKNOWLEDGMENTS

This work has been partly supported by Google Awards.

REFERENCES

1. T. E. Bishop and P. Favaro, "The light field camera: Extended depth of field, aliasing and super-resolution," *IEEE Transactions on PAMI* **34**(5), pp. 972–986, 2012.
2. E. H. Adelson and J. Y. Wang, "Single lens stereo with a plenoptic camera," *IEEE Transactions on PAMI* **14**, pp. 99–106, Feb 1992.
3. R. Ng, M. Levoy, M. Brédif, G. Duval, M. Horowitz, and P. Hanrahan, "Light field photography with a hand-held plenoptic camera," Tech. Rep. CSTR 2005-02, Stanford University, April 2005.
4. M. Levoy, R. Ng, A. Adams, M. Footer, and M. Horowitz, "Light field microscopy," *ACM Trans. Graph.* **25**(3), pp. 924–934, 2006.
5. A. Lumsdaine and T. Georgiev, "Full resolution lightfield rendering," tech. rep., Indiana University and Adobe Systems, 2008.
6. A. Lumsdaine and T. Georgiev, "The focused plenoptic camera," in *ICCP 09 (IEEE Int. Conf. on Computational Photography)*, Apr 2009.
7. A. Levin, W. T. Freeman, and F. Durand, "Understanding camera trade-offs through a Bayesian analysis of light field projections," in *European Conference on Computer Vision*, (14), pp. 619–624, 2008.
8. G. Lippmann, "Epreuves reversibles donnant la sensation du relief," *Journal of Physics* **7**(4), pp. 821–825, 1908.
9. K. Fife, A. El Gamal, and H.-S. Wong, "A 3d multi-aperture image sensor architecture," in *IEEE CICC '06.*, pp. 281–284, 2006.
10. G. Wetzstein, I. Ihrke, D. Lanman, and W. Heidrich, "Computational Plenoptic Imaging," in *Computer Graphics Forum (to appear)*, pp. 1–25, 2011.
11. C. Zhou and S. Nayar, "Computational Cameras: Convergence of Optics and Processing," *IEEE Transactions on Image Processing* **20**, pp. 3322–3340, Dec 2011.
12. A. Levin, W. T. Freeman, and F. Durand, "Understanding camera trade-offs through a bayesian analysis of light field projections," in *Proceedings of the 10th European Conference on Computer Vision: Part IV*, *ECCV '08*, pp. 88–101, Springer-Verlag, (Berlin, Heidelberg), 2008.
13. I. Ihrke, G. Wetzstein, and W. Heidrich, "A theory of plenoptic multiplexing," 2010.
14. C.-K. Liang, G. Liu, and H. H. Chen, "Light field acquisition using programmable aperture camera," in *IEEE ICIP 07*, pp. V233–236, 2007.
15. A. Veeraraghavan, R. Raskar, A. K. Agrawal, A. Mohan, and J. Tumblin, "Dappled photography: mask enhanced cameras for heterodyned light fields and coded aperture refocusing," *ACM Trans. Graph. (Proc SIGGRAPH 2007)* **26**(3), p. 69, 2007.
16. T. Georgeiv and C. Intwala, "Light field camera design for integral view photography," tech. rep., Adobe Systems, 2006.
17. M. Ben-Ezra, A. Zomet, and S. Nayar, "Jitter camera: high resolution video from a low resolution detector," in *IEEE CVPR*, **2**, 2004.
18. W. Cathey and E. Dowski, "New paradigm for imaging systems," *Applied Optics* **41**(29), pp. 6080–6092, 2002.
19. H. Nagahara, S. Kuthirummal, C. Zhou, and S. K. Nayar, "Flexible depth of field photography," in *proc ECCV '08*, Oct 2008.